arXiv:1511.03789v1 [astro-ph.GA] 12 Nov 2015

Ultraviolet Radiative Transfer Modeling of Nearby Galaxies with Extraplanar Dusts

Jong-Ho Shinn[1] and Kwang-Il Seon[1,2,3]

jhshinn@kasi.re.kr

November 13, 2015

Abstract

In order to examine their relation to the host galaxy, the extraplanar dust of six nearby galaxies are modeled, employing a three dimensional Monte Carlo radiative transfer code. The targets are from the highly-inclined galaxies that show dust-scattered ultraviolet halos, and the archival *Galaxy Evolution Explorer* FUV band images were fitted with the model. The observed images are in general well reproduced by two dust layers and one light-source layer, whose vertical and radial distributions have exponential profiles. We obtained several important physical parameters, such as star formation rate (SFR_{UV}), face-on optical depth, and scale-heights. Three galaxies (NGC 891, NGC 3628, and UGC 11794) show clear evidence for the existence of extraplanar dust layer. However, it is found that the rest three targets (IC 5249, NGC 24, and NGC 4173) do not necessarily need a thick dust disk to model the ultraviolet (UV) halo, because its contribution is too small and the UV halo may be caused by the wing part of the *GALEX* point spread function. This indicates that the galaxy samples reported to have UV halos may be contaminated by galaxies with negligible extraplanar (halo) dust. The galaxies showing evidence of the extraplanar dust layer fall within a narrow range on the scatter plots between physical parameters such as SFR_{UV} and extraplanar dust mass. Several mechanisms possible to produce the extraplanar dust are discussed. We also found a hint that the extraplanar dust scale-height might not be much different from the polycyclic aromatic hydrocarbon *emission* characteristic height.

[1]Korea Astronomy and Space Science Institute, 776 Daeduk-daero, Yuseong-gu, Daejeon, 305-348, the Republic of Korea

[2]Astronomy and Space Science Major, Korea University of Science and Technology, 217 Gajeong-ro, Yuseong-gu, Daejeon, 305-350, the Republic of Korea

[3]Department of Astrophysical Sciences, Princeton University, Princeton NJ 08544, USA

Subject headings: radiative transfer — (ISM:) dust, extinction — galaxies: ISM — galaxies: spiral — galaxies: star formation — galaxies: halos

1. Introduction

Galaxies evolve circulating their mediums between disks and halos, through stellar winds and radiation, supernova explosions, dynamic interactions between galaxies, gravitational attraction towards the galactic plane, star formation by gravitational collapse, etc (cf. Finkbeiner 2014). These circulating mediums thus embed important information regarding how the energy is transported and how the raw material for star formation are distributed within the galaxies and their surroundings. Dust is one of such mediums, and it plays several important roles. For instance, it attenuates the stellar light through the scattering and absorption processes, and re-radiates the absorbed light in longer wavelengths to transform the spectral energy distribution of the galaxy (cf. Conroy 2013).

The dust that is located above the galactic plane (say, $z \gtrsim$ a few percent of the galactic diameter), i.e. the extraplanar dust, is especially important in several aspects. First, its existence means that the dust is somehow elevated against, or accreted by, the galactic plane's gravity (cf. Howk 2012). Second, it may reveal the evolutionary connection between the star-forming galaxies and the starburst galaxies, where the star-formation activity can supply the force defying the galactic plane's gravity. Third, it may hold some hints on the dust supplying channel to the circumgalactic medium and the intergalactic medium, where the existence of dust was reported (e.g. Ménard et al. 2010; Zaritsky 1994; McGee & Balogh 2010; Chelouche et al. 2007). Fourth, its existence is intriguing in consideration of the possibility that the extraplanar warm ionized medium (or diffuse ionized gas, Haffner et al. 2009) could be substantially contaminated by the dust-scattered Hα emission (cf. Seon & Witt 2012).

The extraplanar dust has been observed for many edge-on spiral galaxies. The edge-on galaxies reveal the extraplanar dust through the extinction of background stellar light (Howk & Savage 1997, 1999, 2000; Alton et al. 2000; Rossa & Dettmar 2003; Thompson et al. 2004), the mid-infrared continuum (Burgdorf et al. 2007), and ultraviolet (UV) scattered light (Hodges-Kluck & Bregman 2014; Seon et al. 2014). Indirect evidences from the emission of polycyclic aromatic hydrocarbon (PAH) were also reported (McCormick et al. 2013; Irwin & Madden 2006). However, most of previous studies analyzed the data without a physical modeling for the galaxy, and therefore it was hard to extract direct links between physical parameters. For example, the correlation study using the extraplanar PAH emission characteristic height, presented by McCormick et al. (2013), could be misled by the

dilution of radiation field away from the galactic plane, because the PAH emission is *excited* by the absorption of starlight (Draine 2003; Allamandola et al. 1989; Leger & Puget 1984) and hence the emission does not directly correspond to the actual PAH amount. It is also true that a scale-height of the scattered light above the galactic plane is not the same as the actual scale-height of the extraplanar dust layer.

Recently, from the radiative transfer simulation of the UV images, Seon et al. (2014) showed that the extraplanar dust of NGC 891 can properly be modeled by adding a geometrically-thick dust layer. They derived several important physical parameters such as star formation rate (SFR) and dust scale-height, and listed two primary elevation mechanisms for the extraplanar dust: stellar radiation pressure or (magneto)hydrodynamic flows (Howk & Savage 1997; Ferrara et al. 1990; Greenberg et al. 1987). We here extend their approach to the highly-inclined spiral galaxies with dust-scattered UV halos, discovered by Hodges-Kluck & Bregman (2014), in order to investigate if there is any relation between the properties of extraplanar dust and host galaxy. Six targets were analyzed, and three of them found to need no additional thick dust disk in modeling the UV halos. The rest three that need the thick dust disk fall within a narrow range over the scatter plots between several physical parameters such as $\mathrm{SFR_{UV}}$ and extraplanar dust mass.

2. Target, Instrument, and Data Reduction

We are interested in modeling and characterizing the extraplanar dust with several physical parameters. Seon et al. (2014) showed that the extraplanar dust of NGC 891 can be described by the exponential distributions of starlight source and dust. Among the spiral galaxies studied by Hodges-Kluck & Bregman (2014), we selected the galaxies that seem to be properly modeled with the exponential distributions. Those galaxies with ring structures or prominent spiral arms were excluded. Table 1 lists the six selected targets. Their distance, major axis size, stellar mass, and SFR range $\sim 5-75$ Mpc, $\sim 10-50$ kpc, $\sim (0.1-7.0)\times10^{10}$ $M_\odot$, and $\sim 0.1-5.0$ $M_\odot$ yr^{-1}, respectively.

We employed the archival data[1] of *Galaxy Evolution Explorer* (*GALEX*; Martin et al. 2005). *GALEX* was a satellite mission that performed all-sky imaging and spectroscopic survey in two UV bands: FUV (∼1350–1750 Å) and NUV (∼1750–2750 Å). Table 2 shows more detailed information on *GALEX*. The archive provides fully reduced data, and the data reduction pipeline is described in Morrissey et al. (2007). We used the intensity maps, for which no background subtraction was applied during the data reduction. The FUV images

[1]GR6/GR7; `http://galex.stsci.edu/GR6/`

were solely used to model the extraplanar dust, because the FUV band has a narrower bandwidth than the NUV band, and does not include the 2175 Å bump which might cause the sudden variation of dust grain albedo (Figure 1, cf. Draine 2003). Furthermore, the FUV image has a smaller number of foreground point sources than the NUV image, which makes the point-source masking process easier. Table 3 shows the exposure times of individual targets at each band; the NUV exposure time is also shown for reference.

In order to render the intensity maps suitable for two dimensional fitting, we applied additional processes as follows. First, we masked point-like sources, employing the SExtractor (Bertin & Arnouts 1996) output provided by the archive. Other remaining point-like sources were masked manually, and then the blank sky and the target galaxy were left intact. Second, we rotated the masked image for the major axis of the galaxy to be placed horizontal, and cropped the rotated image. These rotating and cropping were implemented using IRAF (Tody 1986, 1993). Finally, we subtracted the linear sky background that have a gradient along the galaxy's minor axis direction. This background was derived by fitting the averaged vertical profile of the cropped image with a linear function. During the fitting, we excluded the central part where the features from the galaxy and extraplanar diffuse sources are not negligible. Figure 2 shows the resultant FUV images and their vertical profiles, which reveal the existence of UV halos.

3. Analysis and Results

3.1. Fitting the *GALEX* FUV images with a three dimensional radiative transfer model

We are interested in the physical properties of the extraplanar dust layer, such as the scale-height and the optical depth. Several physical parameters of the extraplanar dust layer are derived by exploiting three dimensional radiative transfer model to fit the *GALEX* FUV image processed as described in section 2. We used a three dimensional Monte Carlo radiative transfer code of Seon et al. (2014), which models multiple scattering of photons in a cylindrical coordinate system. It uses the "forced first scattering" technique to enhance the calculation efficiency in optically thin media and the "peel-off" technique to generate an image towards the observer (see Steinacker et al. 2013 for more about the computational acceleration techniques). The code also employs a fast voxel traversal algorithm (Amanatides et al. 1987), as implemented in Seon (2015).

The model configuration was the same as in Seon et al. (2014). We adopted the axisymmetric distribution of dust and starlight source, and their radial and vertical profiles follow

the exponential curves[2]. The dust component has two layers which share the same physical parameters except the scale-height and optical depth: one has a smaller scale-height (geometrically thin), while the other has a larger one (geometrically thick). In brief, the following equations represent the dust and starlight distributions.

$$\kappa(r,z) = \begin{cases} \kappa_0^{\rm thin} \exp\left(-\frac{r}{h_d} - \frac{|z|}{z_d^{\rm thin}}\right) + \kappa_0^{\rm thick} \exp\left(-\frac{r}{h_d} - \frac{|z|}{z_d^{\rm thick}}\right), \text{ for } r \le R_d,\ z \le Z_d \\ 0, \text{ for } r > R_d,\ z > Z_d \end{cases} \quad (1)$$

$$I(r,z) = \begin{cases} I_0 \exp\left(-\frac{r}{h_s} - \frac{|z|}{z_s}\right), \text{ for } r \le R_s \\ 0, \text{ for } r > R_s \end{cases} \quad (2)$$

$\kappa(r,z)$ and $I(r,z)$ are the distributions of extinction coefficient and starlight source, respectively. We set the starlight wavelength to be the effective wavelength of *GALEX* FUV band, 1538.6 Å (Morrissey et al. 2007). r and z are the cylindrical coordinates. $z_d^{\rm thin}$, $z_d^{\rm thick}$, and z_s are the scale-heights of geometrically thin and thick dust layers, and starlight sources, respectively. h_d and h_s are the scale-lengths of the dust layer and starlight, respectively. $\kappa_0^{\rm thin}$ and $\kappa_0^{\rm thick}$ are the extinction coefficients at the center of the galaxy ($r = 0$, $z = 0$) of the thin and thick dust layers, respectively. Note that the optical depth along the symmetric axis is $\tau = \tau^{\rm thin} + \tau^{\rm thick} = 2\kappa_0^{\rm thin} z_d^{\rm thin} + 2\kappa_0^{\rm thick} z_d^{\rm thick}$. R_d and R_s are the truncation radii of the dust layers and the starlight, respectively. Z_d is the truncation height of the dust distribution.

For the light scattering calculation, we used the Henyey-Greenstein phase function (Henyey & Greenstein 1941) and adopted the anisotropy parameter and albedo from the R_V=3.1 Milky Way dust model of Draine (2003) and Weingartner & Draine (2001). The modeled image was convolved with the instrumental point spread function (PSF), before comparing with the processed *GALEX* FUV image. In the present paper, the observed images were not folded about the minor axis during the comparison, whereas those were folded in Seon et al. (2014).

The model fitting was performed through χ^2 minimization. We adopted an equal error for all image pixels to give the equal weights for the disk and halo during the fitting, and the error was estimated from the pixel value fluctuation at backgrounds. Since $z_d^{\rm thick}$ is our main interest, we surveyed several fixed parameter space of ($z_d^{\rm thin}$, $z_d^{\rm thick}$; for $z_d^{\rm thin} < z_d^{\rm thick}$) and searched for the best fit parameters. $z_d^{\rm thin}$ ranges from 0.025 kpc to 0.275−0.375 kpc with a 0.05 kpc step, while $z_d^{\rm thick}$ ranges from 0.1 kpc to 2.6−3.6 kpc with a 0.5 kpc step. Table 4 shows the best-fit model parameters for individual targets, and Figure 3 shows the

[2]For the vertical profile, it may be hard to distinguish the exponential type from the power-law type, unless the signal-to-noise ratio is high enough at the distant area from the galactic plane. We note that a power-law *radial* profile was adopted in Ménard et al. (2010) and Hodges-Kluck & Bregman (2014).

corresponding model images. The χ^2 differences between the minimum and its surrounding ($z_d^{\rm thin}$, $z_d^{\rm thick}$) are much larger than one. Thus, the 1-σ uncertainties of scale-heights are much smaller than their step sizes.

The best-fit models have $z_d^{\rm thin}$ of $\sim 0.1-0.4$ kpc and $z_d^{\rm thick}$ of $\sim 0.6-3.1$ kpc. This $z_d^{\rm thin}$ range is comparable to the values from previous optical and near infrared (NIR) studies on the galactic disks with a single dust layer (Xilouris et al. 1998, 1999; Alton et al. 2004). $\tau_B^{\rm thin}$ and $\tau_B^{\rm thick}$ range $\sim 0.4-1.2$ and $\sim 0.01-1.0$, respectively. $\tau_B^{\rm thin}$ is greater than $\tau_B^{\rm thick}$ for all targets except NGC 24. The $\tau_B^{\rm thin}$ range is comparable to the values from previous optical and NIR studies (Xilouris et al. 1998, 1999; Alton et al. 2004). z_s ranges $\sim 0.1-0.2$ kpc, which is lower than the values from previous optical studies ($\sim 0.2-0.5$ kpc, Xilouris et al. 1998, 1999). This may reflect the fact that early-type stars, which are bright in UV, have a lower scale-height than late-type stars (e.g. Bahcall & Soneira 1980; Wainscoat et al. 1992). SFR was estimated from the intrinsic UV luminosity, employing the Starburst99 (Leitherer et al. 1999). The Salpeter initial mass function was assumed in calculating the UV luminosity per unit SFR. We also assumed that our sample galaxies are in a steady and continuous star-forming phase. The derived SFRs ($\rm SFR_{UV}$) are comparable with the SFRs derived from the infrared luminosity ($\rm SFR_{IR}$, Figure 4)[3], although $\rm SFR_{UV}$ is a little lower than $\rm SFR_{IR}$. We note that the estimated $\rm SFR_{UV}$ includes some uncertainties, in the sense that the Starburst99 model is based on several (probable) assumptions, for instance, in star formation history and metallicity, and the assumption we made in the radiative transfer modeling—smooth distribution of dust and light source—is a simplified representation of galaxies.

We note that the obtained fitting parameters for NGC 891 are comparable in general to the $\tau_B^{\rm thin}=0.9$ case values of Seon et al. (2014). This shows that our parameter search method over ($z_d^{\rm thin}$, $z_d^{\rm thick}$) grids returns a coherent output. IC 5249's h_s is much larger than others, and this peculiarity may be related with its very flat appearance (Fig. 3a). NGC 24 has the highest $\tau_B^{\rm thick}$, $z_d^{\rm thick}$ and lowest h_d, $\rm SFR_{UV}$, and is the least edge-on. NGC 3628 has the highest $\rm SFR_{UV}$. It has many local features, but the global shape is well reproduced by the model (Fig. 3d). NGC 4173 has the lowest $z_d^{\rm thick}$. UGC 11794 has the smallest angular size, and hence the data quality is the lowest among our targets. However, the fit results give reasonable parameters.

---

[3]$\rm SFR_{IR}$ is omitted for IC 5249 and NGC 4173, because there is no far-infrared data that can be used in the SFR estimation (see Table 1). For example, they are not listed in the catalog of *Herschel* and *AKARI*.

3.1.1. Effects of radially extended PSF on the model fitting

When observing astronomical objects, optical systems inevitably accompany scattered lights, which are characterized by the wing part of PSF. It was recently claimed that a radially extended PSF should be used in the analyses, if the low surface-brightness features around bright sources are the targets of interest (Sandin 2014, 2015); Sandin (2014) found that the PSF radius should be larger than 1.5 times the distance between the low surface-brightness feature and bright source. Some of our targets have UV halos extended up to $\sim 150''$ from the galactic plane (see Figure 2), which is larger than the radius of the *GALEX* standard PSF ($\sim 90''$). Therefore, we check if the extended wing part of PSF could have significant effects on the model fitting.

Since the extended PSF of *GALEX* does not exist, we synthesized an extended PSF from the radial profile of standard PSF. We fitted the average radial profile of standard PSF with two functions referring Racine (1996): eq. (6) of (Racine 1996, the Moffat function) for the core and eq. (7) of Racine (1996) for the wing. The fitting was performed on the standard PSF cutting at the radius of $60''$ due to the larger fluctuation at higher radius. Figure 5 shows the fit result which extends up to the radius of $250''$. The ratio of wing/core at the origin is about 2×10^{-3}, and the characteristic angular scales are $4.46''$ and $15.8''$ for the core and wing parts, respectively. From this extended radial profile, we made a synthetic, extended PSF whose radial extent reaches $250''$.

In order to visualize the effects of extended PSF on the galactic halo, we made plots of profiles averaged along the horizontal axes, as seen in Figure 6. The *red-dashed* and *magenta-solid* lines are the best-fit model profiles, convoluted with the *extended* and *standard* PSFs, respectively, excluding the thick dust disk component (see eq. (1)). If the UV halo is caused by the extended PSF wing rather than the extraplanar dust, the *red-dashed* line must significantly be higher than the *magenta-solid* line at the region above the background noise upper bound (*black-dotted* line in Figure 6). We found that the *red-dashed* lines are higher than the *magenta-solid* line at the region *below or marginally above* the noise upper bound for all targets. This result seems to be due to that the most contribution of PSF wing part is already included in the standard PSF, whose radial extent is $\sim 90''$, and that the background signal-to-noise ratio of *GALEX* FUV data is not high enough to reveal the extended wing contribution.

The vertical profiles of NGC 891, NGC 3628, and UGC 11794 clearly show the halo emission excess which cannot be explained with the PSF wing. However, we found that the existence of thick dust disk is questionable for the rest three targets—IC 5249, NGC 24, and NGC 4173. As Figure 6 shows, for these targets, the *magenta-solid* line is hardly distinguishable from the *black-solid* line, the profile from the best-fit model including both

thin and thick dust disks (see eq. (1)) and being convoluted with the standard PSF. These targets have lower $\tau_B^{\rm thick} \times (h_d^{\rm thick})^2$ than other targets (see Table 4), which indicates having lower amount of the extraplanar dust (see section 3.2) and subsequently makes the two profiles indistinguishable. In the case of NGC 24, its less edge-on appearance makes the difference even weaker. These three targets were excluded from our further analyses.

We here note that some of the galactic UV halos reported by Hodges-Kluck & Bregman (2014) may be explainable *with the thin dust disk solely*. The data profiles of IC 5249 and NGC 24 seen in Figure 6 show hints of extended, decreasing wing-like features, but with intensities comparable to or lower than the background upper bound. The feature for IC 5249 can be explained by the *standard* PSF wing solely. However, for NGC 24, the *extended* PSF seems to reproduce the profile better. It should be noted that the wing features caused by the PSF can be misidentified as extended UV halos, without the aid of detailed modeling that properly includes the PSF effects.

3.2. Extraplanar dust and the host-galaxy radiation

Since our main interest is to investigate the relation between properties of the extraplanar dust and the host galaxy, we first check whether or not there is any correlation between the extraplanar dust mass (M_{ext}) and $\rm SFR_{UV}$. The extraplanar dust was defined to be the dust located outside a certain vertical distance (z_x) from the galactic plane. We set z_x to be 5% of the major axis size (D_{25}); for example, NGC 891 has $z_x \simeq 2$ kpc (see Table 5). M_{ext} is estimated as follows. We integrate the extinction coefficient over the extraplanar volume, where $0 \leq r \leq R_d$ and $z_x \leq z \leq Z_d$ (cf. eq. (1)). This returns a value proportional to $\tau_B\, h_d^2$, which is converted to M_{ext}, using the extinction curve from the R_V=3.1 Milky Way dust model of Draine (2003) and Weingartner & Draine (2001).

The top-left panel of Figure 7 shows the scatter plot between $\rm SFR_{UV}$ (Table 4) and M_{ext} estimated as above (Table 5). For reference to galaxy luminosity, the scatter plot between M_{ext} and the galactic stellar mass (M_*) is also plotted in the top-right panel of Figure 7. M_{ext} falls between $10^{-4}M_*$ and $10^{-3}M_*$. We here note that M_{ext} of NGC 891 (8.91×10^6 $M_\odot$ for $|z| > 1.97$ kpc, Table 5) is ~ 40 times larger than that estimated by Alton et al. (2000), 2.1×10^5 $M_\odot$ for $|z| > 0.68$ kpc. This difference is because Alton et al. (2000) only modeled the geometrically thin dust disk. Their dust scale-height of 0.31 kpc is similar to our $z_d^{\rm thin} = 0.325$ kpc (Table 4).

We check another relation between the obtained model parameters, which is thought to be scale-independent, referring to McCormick et al. (2013). The bottom-left panel of

Figure 7 shows a scatter plot between the SFR_{UV} surface density ($\Sigma_{SFR,UV}$) and the ratio of z_d^{thick}/D_{25}. $\Sigma_{SFR,UV}$ is calculated from SFR_{UV} (Table 4) and D_{25} (Table 1). The present results seem to fit into the relationship found by McCormick et al. (2013) over a much larger SFR surface density (Σ_{SFR}) dynamic range, although they used the *PAH-emission* characteristic height instead of the dust scale-height.

We cannot draw any conclusive results about the relation between the aforesaid quantities, since the number of samples is too small (see section 3.1.1). However, note that those quantities fall within a narrow range for all three targets (see Figure 7).

4. Discussion

We found that three of our targets do not need any additional dust disk other than the typical thin dust disk, in modeling the galactic UV halo radiation reported by Hodges-Kluck & Bregman (2014) (see section 3.1.1). Hodges-Kluck & Bregman (2014) showed low and high correlations of the specific halo UV luminosity with the specific SFR and the host-galaxy UV luminosity, respectively. Our result suggests that the relations found by Hodges-Kluck & Bregman (2014) may include some contamination from the galaxies with negligible halo (extraplanar) dust. This also demonstrates how the radiative transfer modeling can contribute to the interpretation of the galactic UV halo radiation.

Since the sample number is too small, it would be premature to make a definite statement based on the scatter plots between different physical quantities (Figure 7). However, even with three targets, Figure 7 shows the quantities fall within a narrow range. We also note that the three targets with no clear evidence of the thick dust layer have much lower SFR_{UV} than the other targets (Table 4). These suggest that a common mechanism might regulate the behavior of extraplanar dust.

First, we can point out the galactic radiation pressure as a plausible mechanism. This mechanism was previously studied by several authors (Ferrara et al. 1991; Franco et al. 1991; Ferrara et al. 1990; Barsella et al. 1989; Greenberg et al. 1987; Pecker 1974, 1972; Chiao & Wickramasinghe 1972). They showed that dust grains can be elevated above the galactic plane and even escaped from the galaxy by the radiation pressure, considering two dust species (silicate and graphite) and diverse dust sizes under various galactic radiation fields and environments. There is a hint that the difference of galactic spectral shape might not significantly alter the strength of the radiation pressure, from the wavelength-averaged radiation pressure coefficient Q_{pr}^* for Sb and Sc type galaxies (Ferrara et al. 1991). If this is the case and our target galaxies share a similar grain size distribution, the main factor that

determines M_{ext} would be the galactic luminosity itself, rather than the spectral shape of the radiation field.

Howk & Savage (1997) listed other elevating mechanisms such as hydrodynamical phenomena, magnetic field effects, dynamical instabilities. They exemplified galactic fountain flows (Bregman 1980; Houck & Bregman 1990), Parker instability by horizontal magnetic field (Parker 1966), and vertical instability by non-axisymmetric potentials (Binney 1981; Mulder & Hooimeyer 1984). However, we think that all three mechanisms have some difficulties in directly producing the observed global-and-diffuse UV halos (Hodges-Kluck & Bregman 2014), because their activities are likely to be local, not widespread over the disk.[4] In the case of galactic fountain, the hot gas which is shock-heated by supernova explosions may be able to spread dust over the galactic halo somewhat evenly due to their high mobility, if the dust dragging by the hot gas is strong enough. The galactic radiation may have some advantage in producing the global-and-diffuse UV halo, since the radiation propagates approximately plane-parallel away from the galactic plane. It should be noted that many UV bright features close to the galactic mid-plane were found to correlate with star-forming regions in the mid-plane, especially for NGC 891 (Seon et al. 2014). These bright, scattered features might be due to the local mechanisms, as for the filamentary absorption features observed by Howk & Savage (1997).

Another possible mechanism is the dust accretion from the circumgalactic or intergalactic medium. The existence of dust in the circumgalactic and intergalactic medium has been known from previous studies (e.g. Ménard et al. 2010; Zaritsky 1994; McGee & Balogh 2010; Chelouche et al. 2007). Therefore, if this external dust accretes to the host galaxy by the gravitational attraction (cf. Oosterloo et al. 2007), the extraplanar dust can be formed for the host galaxy. However, it is not clear whether the accretion process can make the diffuse-and-global distribution of extraplanar dust, including the PAH molecules. We here note that the diffuse UV halo radiation reported by Hodges-Kluck & Bregman (2014) can have some localized features unresolved by *GALEX* and *Swift*, whose spatial resolutions are $\sim 2-5''$.

Other relations between the extraplanar dust and SFR can be seen from the study of McCormick et al. (2013). They investigated the extraplanar PAH emission of the nearby galaxies with winds or extraplanar diffuse ionized gas, and showed the high correlations between the galactic infrared flux and the extraplanar PAH flux ($r = 0.89$), and between $\Sigma_{\rm SFR}$ and the ratio of PAH emission characteristic height over galactic major axis size ($H_{\rm ePAH}/D_{25}$, $r = 0.93$). We here note that the PAH emission strength does not indicate the PAH mass,

[4]Note that these three mechanisms might be applicable to the filamentary, vertical dust features discovered by Howk & Savage (1997).

as mentioned in section 1, since PAH emits infrared radiations absorbing UV and optical radiations (Draine 2003; Allamandola et al. 1989; Leger & Puget 1984). It is therefore improper to directly compare their results with ours (Figure 7). However, $H_{\rm ePAH}$ might not be much different from $z_d^{\rm thick}$, as our ($\Sigma_{\rm SFR,UV}$, $z_d^{\rm thick}/D_{25}$) data points shows no prominent deviation from the linear relation between $\Sigma_{\rm SFR}$ and $H_{\rm ePAH}/D_{25}$ of McCormick et al. (2013). Our $\Sigma_{\rm SFR,UV}$ ($\sim 10^{-3}\ M_\odot\ {\rm yr}^{-1}\ {\rm kpc}^{-2}$) is located at the lower range of their $\Sigma_{\rm SFR}$, and thus a future study on combined targets may reveal the connection of extraplanar dust with the star-forming and star-bursting galaxies. If we extends the targets to include the galaxies in the vicinity of intergalactic dust (e.g. Ménard et al. 2010; Zaritsky 1994; McGee & Balogh 2010; Chelouche et al. 2007), we could study the dust at whole scales, i.e. from circumgalactic to intergalactic scales.

5. Conclusions

We modeled the extraplanar dust of six nearby galaxies, employing three dimensional radiative transfer Monte-Carlo simulation code, so as to investigate the relations with their host galaxy's property. The targets were selected from the highly-inclined galaxies that show dust-scattered UV halos (Hodges-Kluck & Bregman 2014), and the archival *GALEX* FUV band images were used. The configurations of dust and starlight sources are the same as Seon et al. (2014). Two dust layers and one starlight source layer are assumed, and their radial and vertical distributions are all exponential. The FUV images of all six galaxies are well reproduced from the modeling, and we obtained several important physical parameters, such as $\rm SFR_{UV}$, B-band face-on optical depth, and scale-height. However, we found that the UV halo of three targets (IC 5249, NGC 24, and NGC 4173) can be modeled with the typical thin dust disk solely, since the contribution from the thick dust disk is too small. These three targets were excluded from our further analyses, and we made scatter plots between several physical quantities for the rest three targets (NGC 891, NGC 3628, and UGC 11794). Although the sample number is just three, the data points fall within a narrow range in the scatter plots between M_{ext}, $\rm SFR_{UV}$, M_*, $z_d^{\rm thick}/D_{25}$, and $\Sigma_{\rm SFR,UV}$.

The needlessness of the thick dust disk for some galaxies reported to have UV halos by Hodges-Kluck & Bregman (2014) indicates that the sample galaxies of Hodges-Kluck & Bregman (2014) may be contaminated by the galaxies with negligible extraplanar (halo) dust. This may thus affect the relations between the specific halo UV luminosity, the specific SFR, and the specific host-galaxy UV luminosity, they found. Although the sample number is too small, their narrow locations over the scatter plots suggest that a common mechanism may regulate the behavior of the extraplanar dust. We lists several possible mechanisms,

discussing their ability to produce the observed diffuse-and-global UV halos. They are the galactic radiation, the (magneto-)hydrodynamic phenomena, and the dust accretion from circumgalactic or intergalactic medium.

The extraplanar PAH emission study of nearby galaxies by McCormick et al. (2013) could not directly compared with ours, since the PAH emission does not simply mean the amount of PAH; PAH emits infrared radiation absorbing UV and optical radiations (Draine 2003; Allamandola et al. 1989; Leger & Puget 1984). However, $H_{\rm ePAH}$ might not be much different from $z_d^{\rm thick}$, as our ($\Sigma_{\rm SFR,UV}$, $z_d^{\rm thick}/D_{25}$) data points shows no prominent deviation from the linear relation between $\Sigma_{\rm SFR}$ and $H_{\rm ePAH}/D_{25}$ of McCormick et al. (2013). Our $\Sigma_{\rm SFR,UV}$ is at the lower end of McCormick et al.'s (2013) $\Sigma_{\rm SFR}$ range, and hence we will be able to study the connection of extraplanar dust with the star-forming and starburst galaxies, by extending our targets to include theirs.

J.-H.S. is grateful to Yujin Yang, Dennis Zaritsky, and Ann Zabludoff for their valuable comments and discussion on the results.

REFERENCES

Allamandola, L. J., Tielens, A. G. G. M., & Barker, J. R. 1989, ApJS, 71, 733

Alton, P. B., Rand, R. J., Xilouris, E. M., et al. 2000, A&AS, 145, 83

Alton, P. B., Xilouris, E. M., Misiriotis, A., Dasyra, K. M., & Dumke, M. 2004, A&A, 425, 109

Amanatides, J., Woo, A., et al. 1987, in Eurographics '87: Proc. European Computer Graphics Conf. and Exhibition (New York: Elsevier), 3

Bahcall, J. N., & Soneira, R. M. 1980, ApJS, 44, 73

Barsella, B., Ferrini, F., Greenberg, J. M., & Aiello, S. 1989, A&A, 209, 349

Bell, E. F., & de Jong, R. S. 2001, ApJ, 550, 212

Bertin, E., & Arnouts, S. 1996, A&AS, 117, 393

Binney, J. 1981, MNRAS, 196, 455

Bregman, J. N. 1980, ApJ, 236, 577

Burgdorf, M., Ashby, M. L. N., & Williams, R. 2007, ApJ, 668, 918

Chelouche, D., Koester, B. P., & Bowen, D. V. 2007, ApJ, 671, L97

Chiao, R. Y., & Wickramasinghe, N. C. 1972, MNRAS, 159, 361

Conroy, C. 2013, ARA&A, 51, 393

Draine, B. T. 2003, ARA&A, 41, 241

Ferrara, A., Aiello, S., Ferrini, F., & Barsella, B. 1990, A&A, 240, 259

Ferrara, A., Ferrini, F., Barsella, B., & Franco, J. 1991, ApJ, 381, 137

Finkbeiner, A. 2014, Science, 346, 905

Franco, J., Ferrini, F., Barsella, B., & Ferrara, A. 1991, ApJ, 366, 443

Greenberg, J. M., Ferrini, F., Barsella, B., & Aiello, S. 1987, Nature, 327, 214

Haffner, L. M., Dettmar, R.-J., Beckman, J. E., et al. 2009, RvMP, 81, 969

Henyey, L. G., & Greenstein, J. L. 1941, ApJ, 93, 70

Hodges-Kluck, E., & Bregman, J. N. 2014, ApJ, 789, 131

Houck, J. C., & Bregman, J. N. 1990, ApJ, 352, 506

Howk, J. C. 2012, in EAS Publications Series, Vol. 56, EAS Publications Series, ed. M. A. de Avillez, 291–298

Howk, J. C., & Savage, B. D. 1997, AJ, 114, 2463

—. 1999, AJ, 117, 2077

—. 2000, AJ, 119, 644

Irwin, J. A., & Madden, S. C. 2006, A&A, 445, 123

Kennicutt, Jr., R. C. 1998, ApJ, 498, 541

Leger, A., & Puget, J. L. 1984, A&A, 137, L5

Leitherer, C., Schaerer, D., Goldader, J. D., et al. 1999, ApJS, 123, 3

Martin, D. C., Fanson, J., Schiminovich, D., et al. 2005, ApJ, 619, L1

McCormick, A., Veilleux, S., & Rupke, D. S. N. 2013, ApJ, 774, 126

McGee, S. L., & Balogh, M. L. 2010, MNRAS, 405, 2069

Ménard, B., Scranton, R., Fukugita, M., & Richards, G. 2010, MNRAS, 405, 1025

Morrissey, P., Conrow, T., Barlow, T. A., et al. 2007, ApJS, 173, 682

Mulder, W. A., & Hooimeyer, J. R. A. 1984, A&A, 134, 158

Oosterloo, T., Fraternali, F., & Sancisi, R. 2007, AJ, 134, 1019

Parker, E. N. 1966, ApJ, 145, 811

Pecker, J.-C. 1972, A&A, 18, 253

—. 1974, A&A, 35, 7

Racine, R. 1996, PASP, 108, 699

Rice, W., Lonsdale, C. J., Soifer, B. T., et al. 1988, ApJS, 68, 91

Rossa, J., & Dettmar, R. 2003, A&A, 406, 505

Sandin, C. 2014, A&A, 567, A97

—. 2015, A&A, 577, A106

Seon, K.-I. 2015, JKAS, 48, 57

Seon, K.-I., & Witt, A. N. 2012, ApJ, 758, 109

Seon, K.-I., Witt, A. N., Shinn, J.-H., & Kim, I.-J. 2014, ApJ, 785, L18

Skrutskie, M. F., Cutri, R. M., Stiening, R., et al. 2006, AJ, 131, 1163

Steinacker, J., Baes, M., & Gordon, K. D. 2013, ARA&A, 51, 63

Thompson, T. W. J., Howk, J. C., & Savage, B. D. 2004, AJ, 128, 662

Tody, D. 1986, in Society of Photo-Optical Instrumentation Engineers (SPIE) Conference Series, Vol. 627, Instrumentation in astronomy VI, ed. D. L. Crawford, 733

Tody, D. 1993, in Astronomical Society of the Pacific Conference Series, Vol. 52, Astronomical Data Analysis Software and Systems II, ed. R. J. Hanisch, R. J. V. Brissenden, & J. Barnes, 173

Wainscoat, R. J., Cohen, M., Volk, K., Walker, H. J., & Schwartz, D. E. 1992, ApJS, 83, 111

Weingartner, J. C., & Draine, B. T. 2001, ApJ, 548, 296

Xilouris, E. M., Alton, P. B., Davies, J. I., et al. 1998, A&A, 331, 894

Xilouris, E. M., Byun, Y. I., Kylafis, N. D., Paleologou, E. V., & Papamastorakis, J. 1999, A&A, 344, 868

Zaritsky, D. 1994, AJ, 108, 1619

This preprint was prepared with the AAS LaTeX macros v5.2.

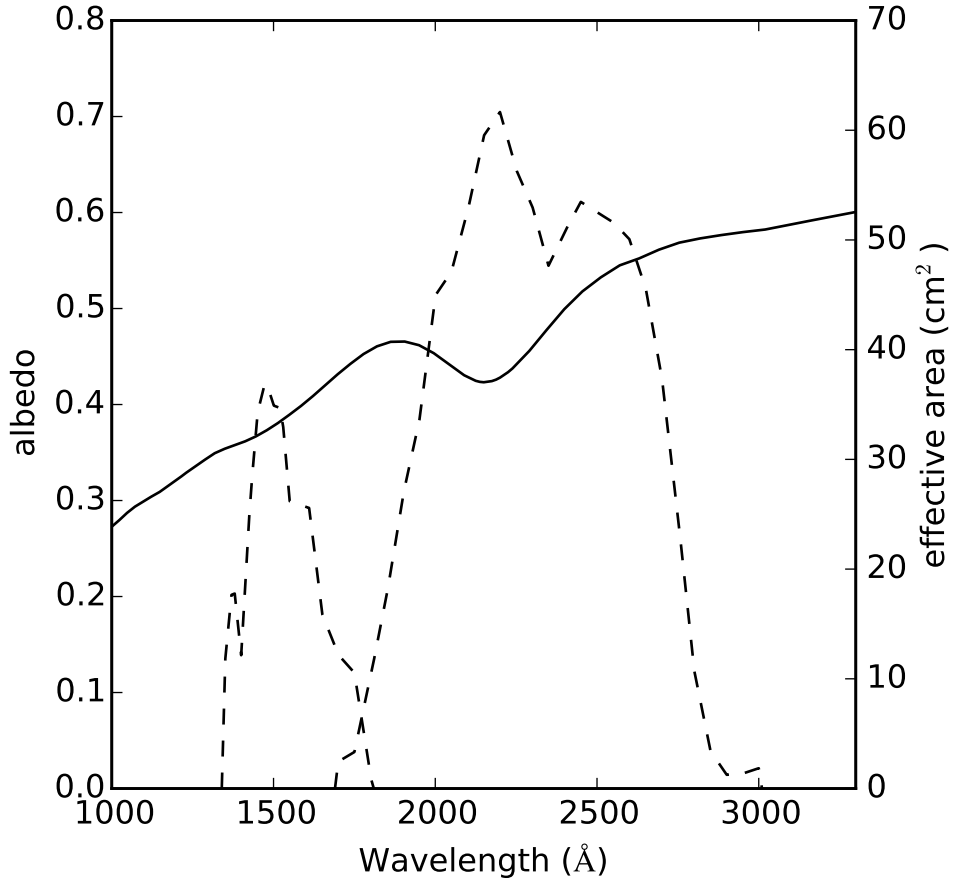

Fig. 1.— The albedo curve from the R_V=3.1 Milky Way dust model of Draine (2003) (solid) and the *GALEX* FUV/NUV effective area curves (dashed).

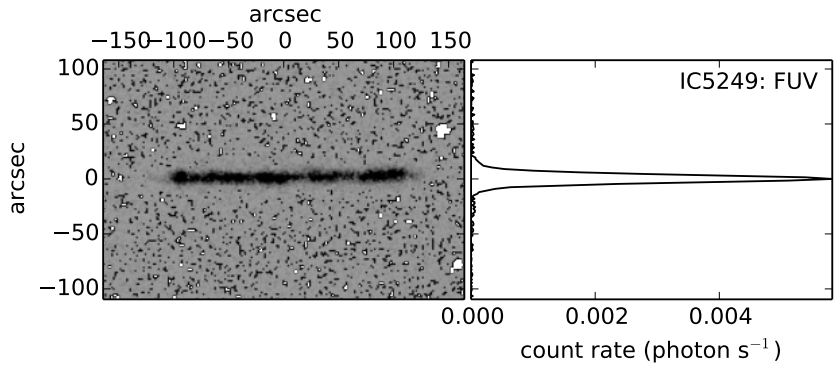

(a)

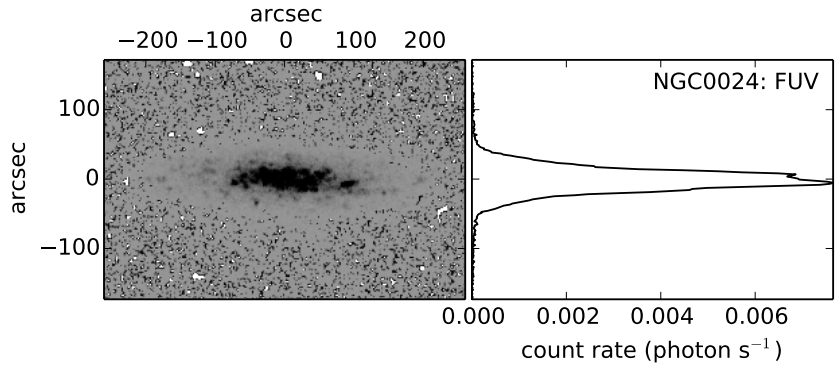

(b)

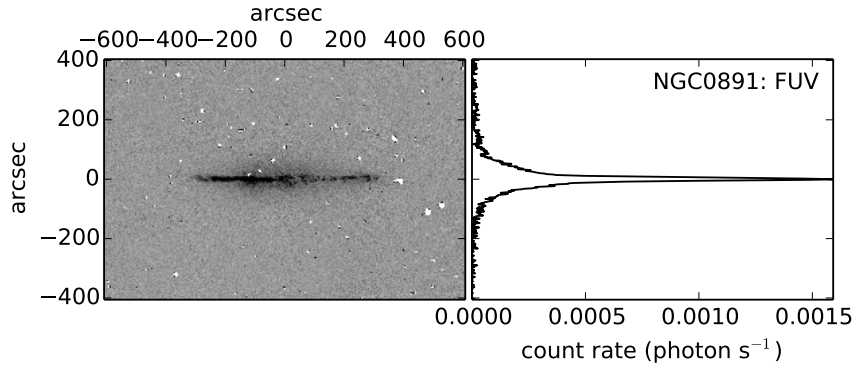

(c)

Fig. 2.— *GALEX* FUV images and vertical profiles of our target galaxies.

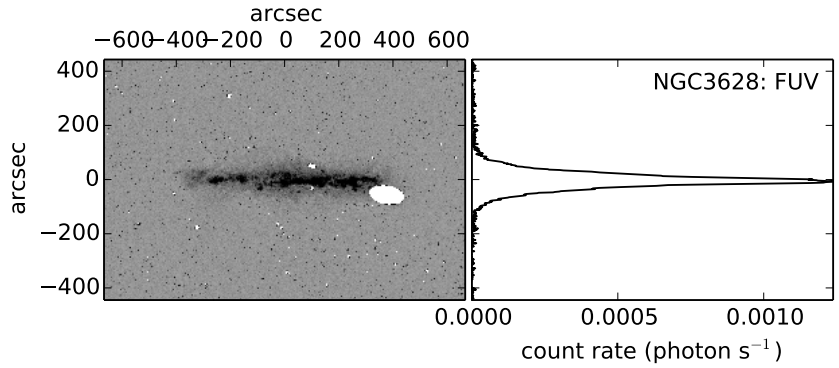

(d)

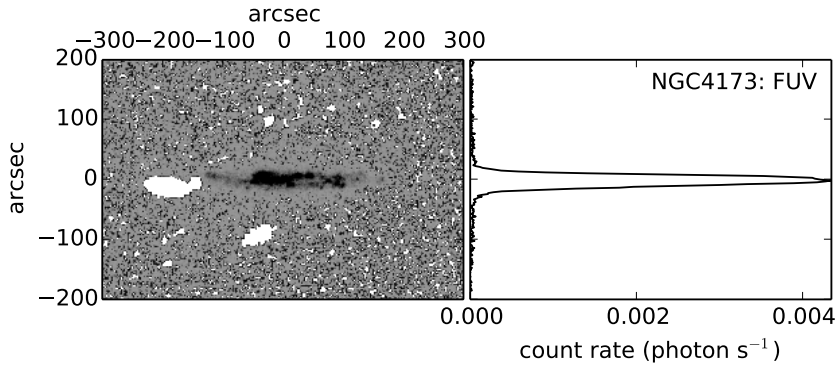

(e)

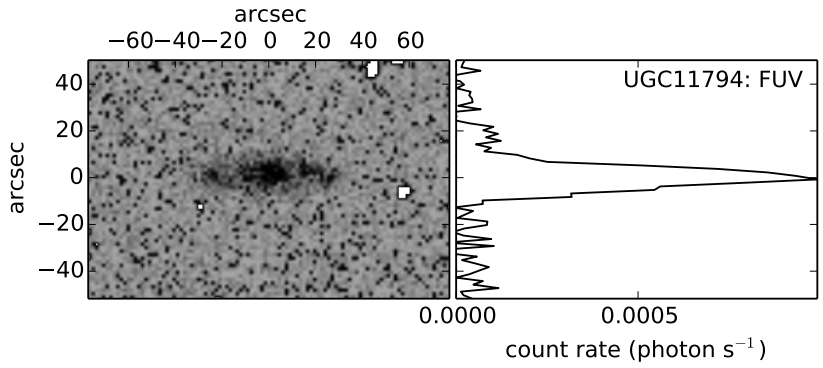

(f)

Fig. 2.— Continued.

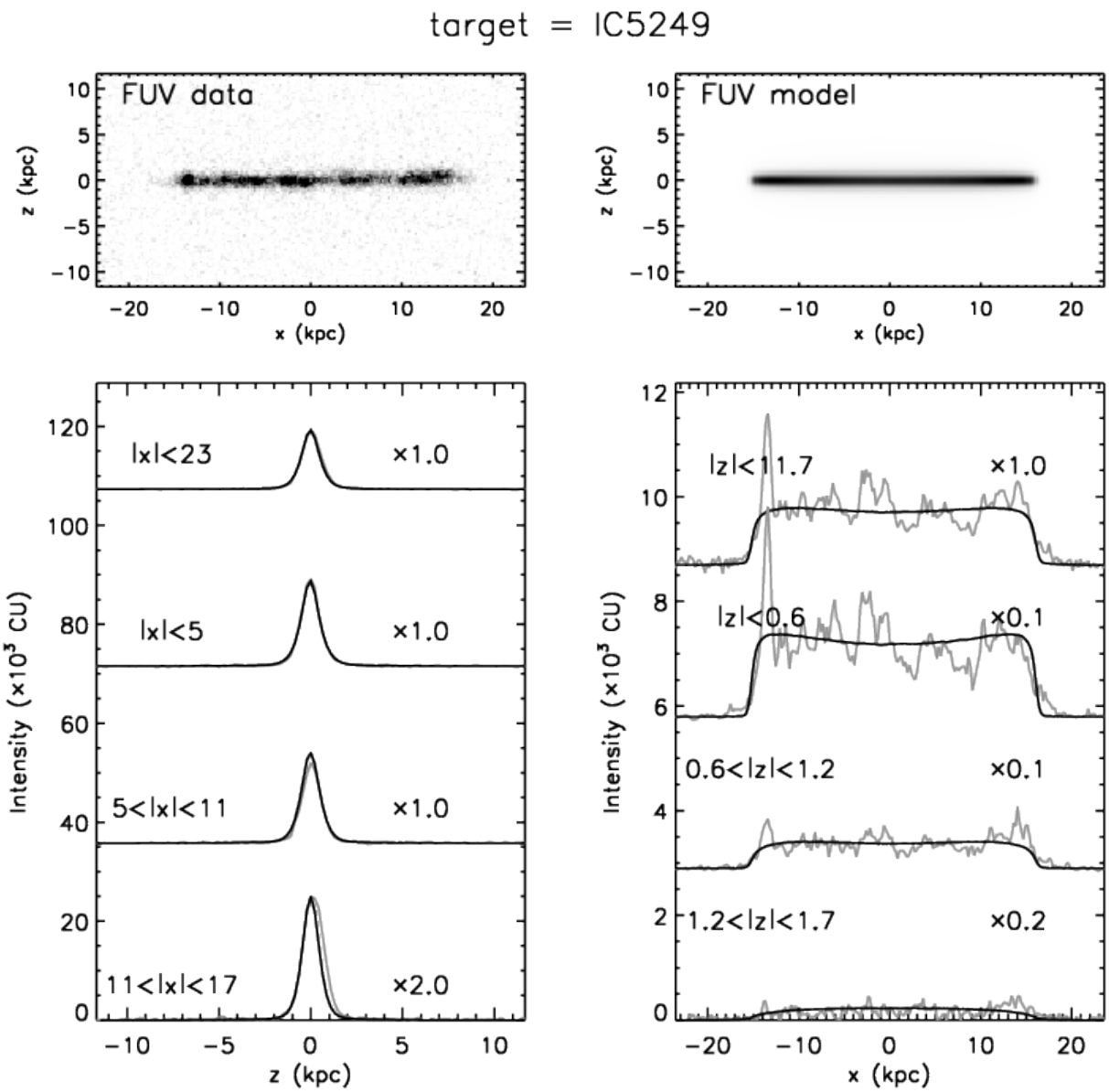

(a)

Fig. 3.— Fitting results. (*upper-left*) *GALEX* FUV image. (*upper-right*) modeled image. (*lower-left*) vertical profiles (*lower-right*) horizontal profiles. The profiles of the modeled image are black lines, while those of *GALEX* FUV images are gray lines. (a)-(f) best-fit results for individual targets.

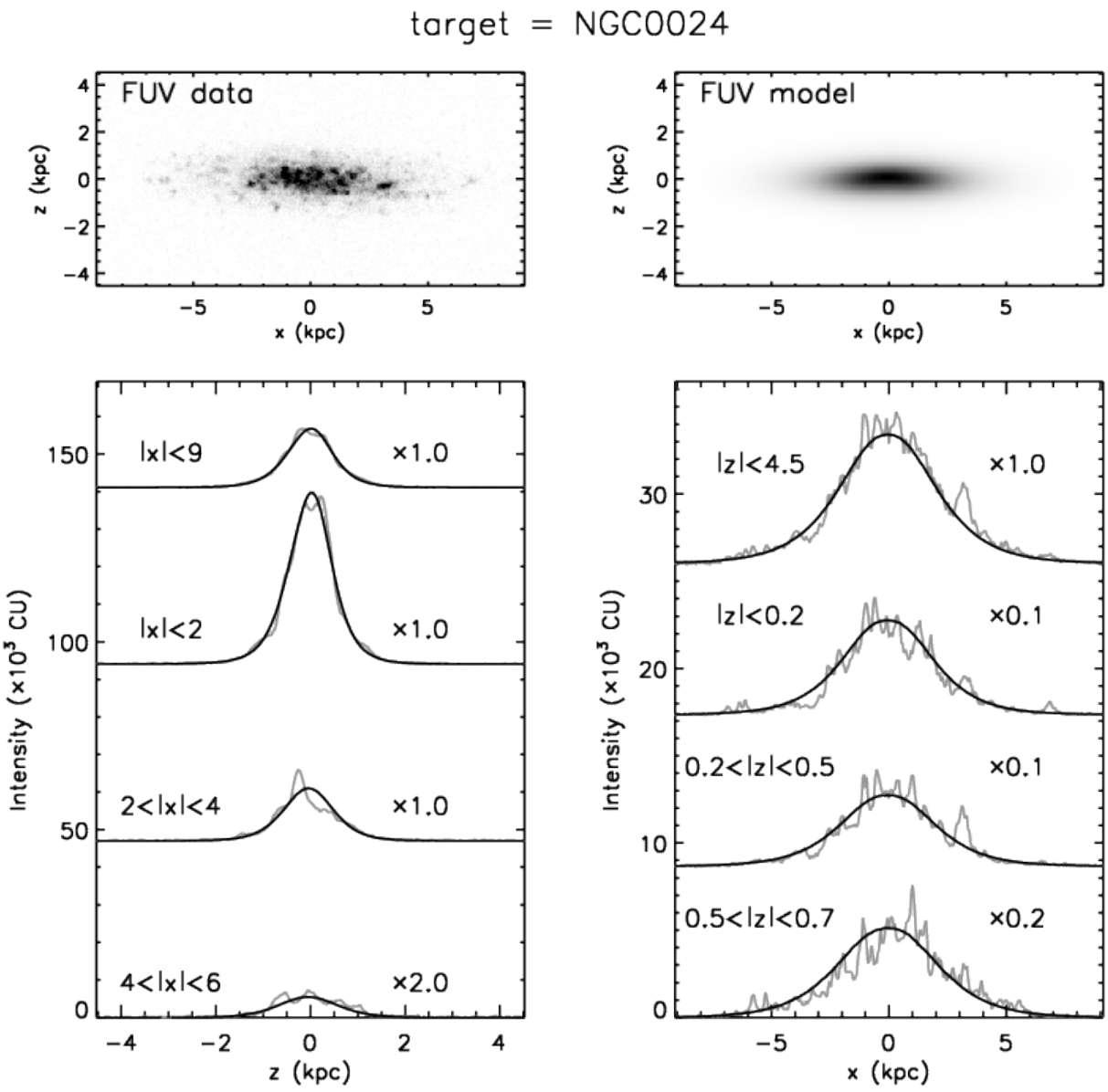

(b)

Fig. 3.— Continued.

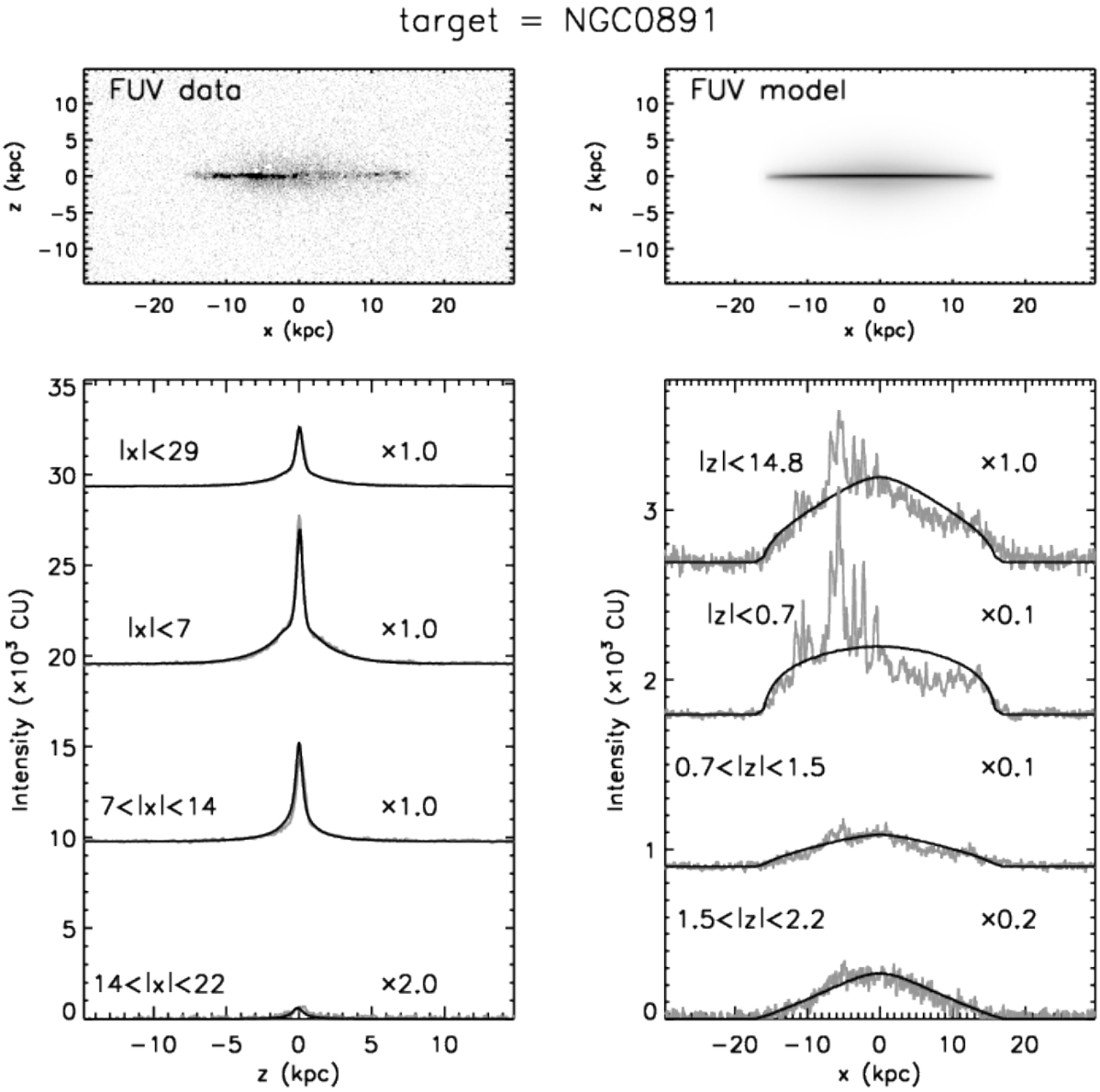

(c)

Fig. 3.— Continued.

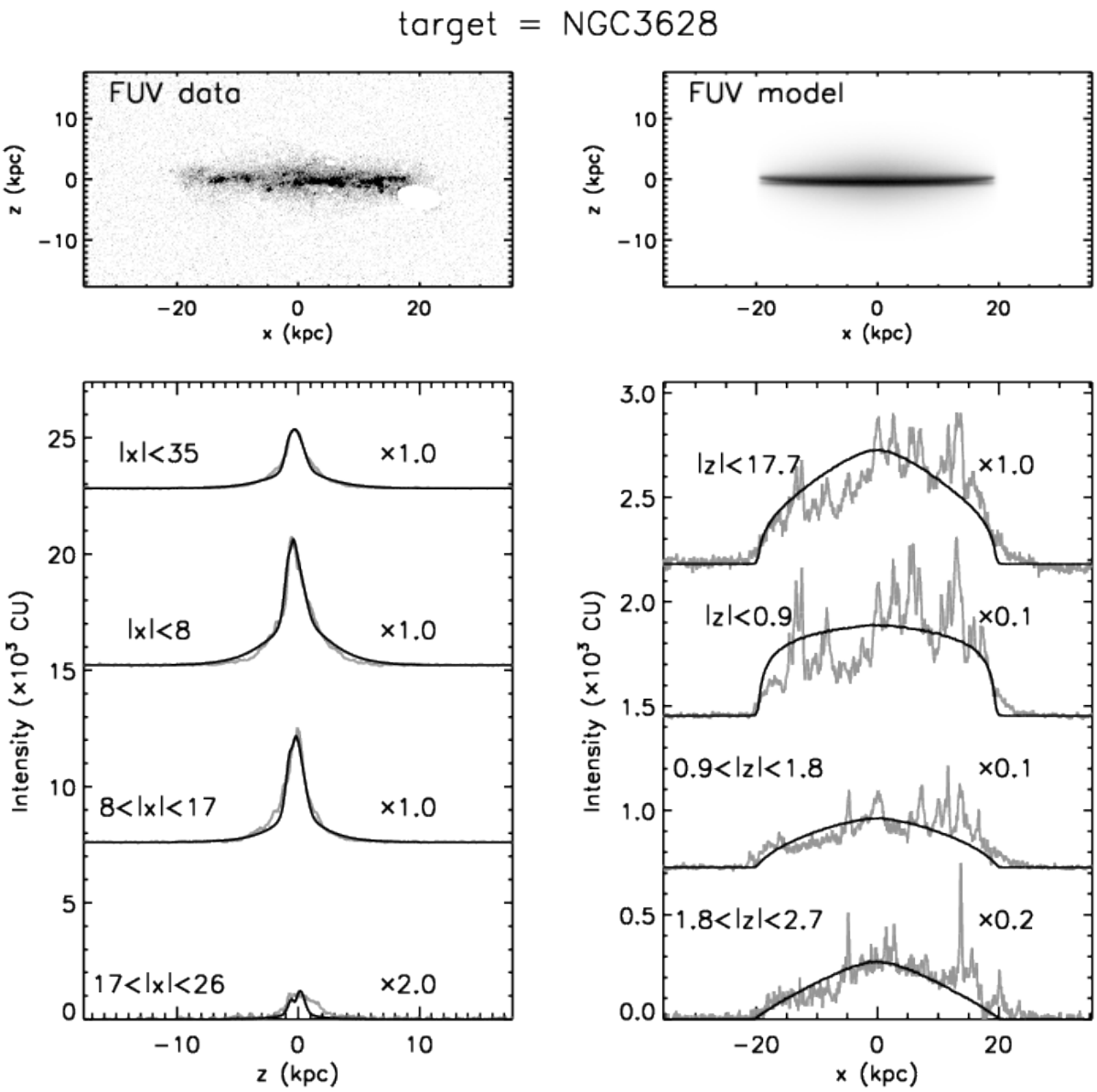

(d)

Fig. 3.— Continued.

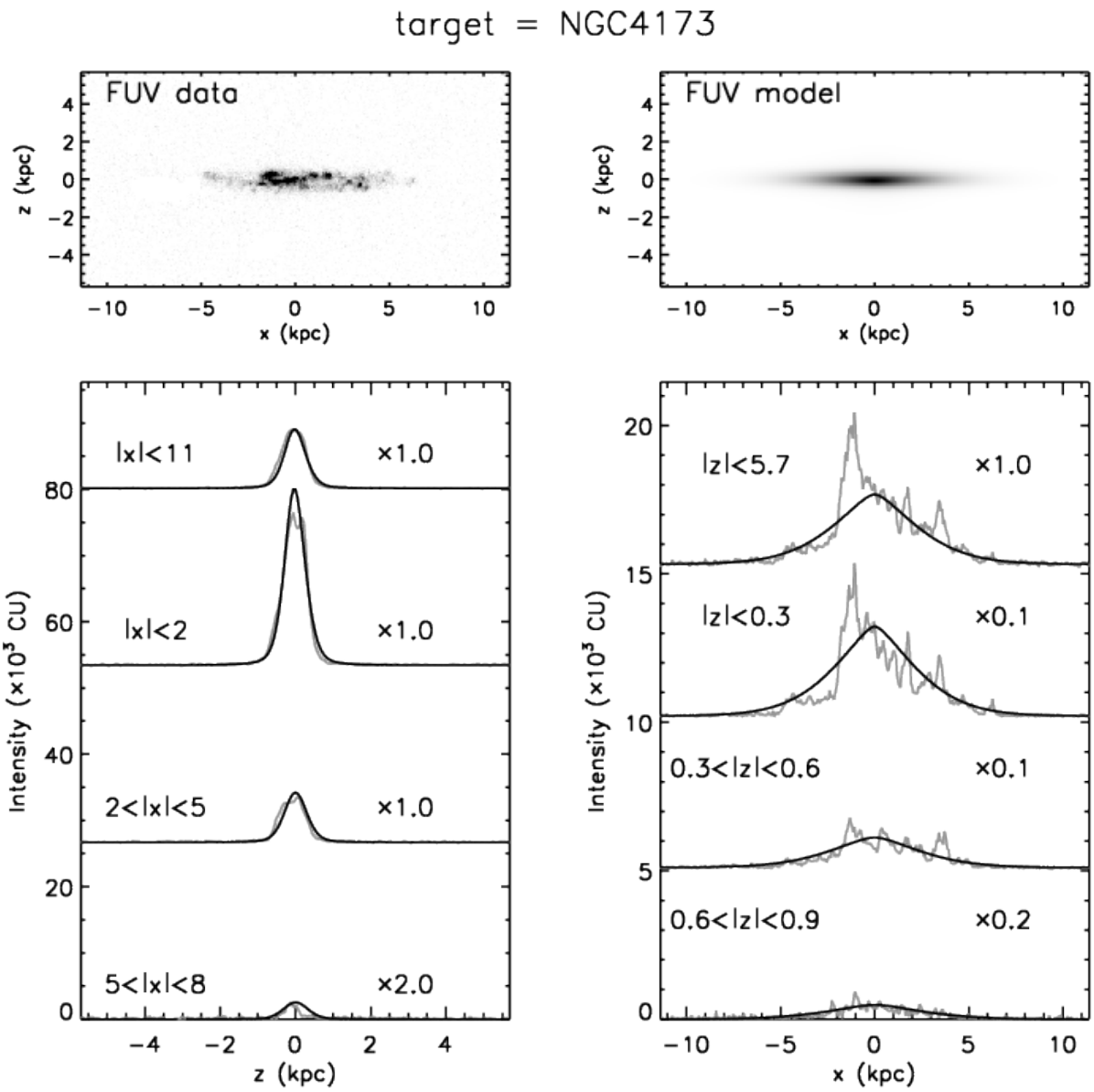

(e)

Fig. 3.— Continued.

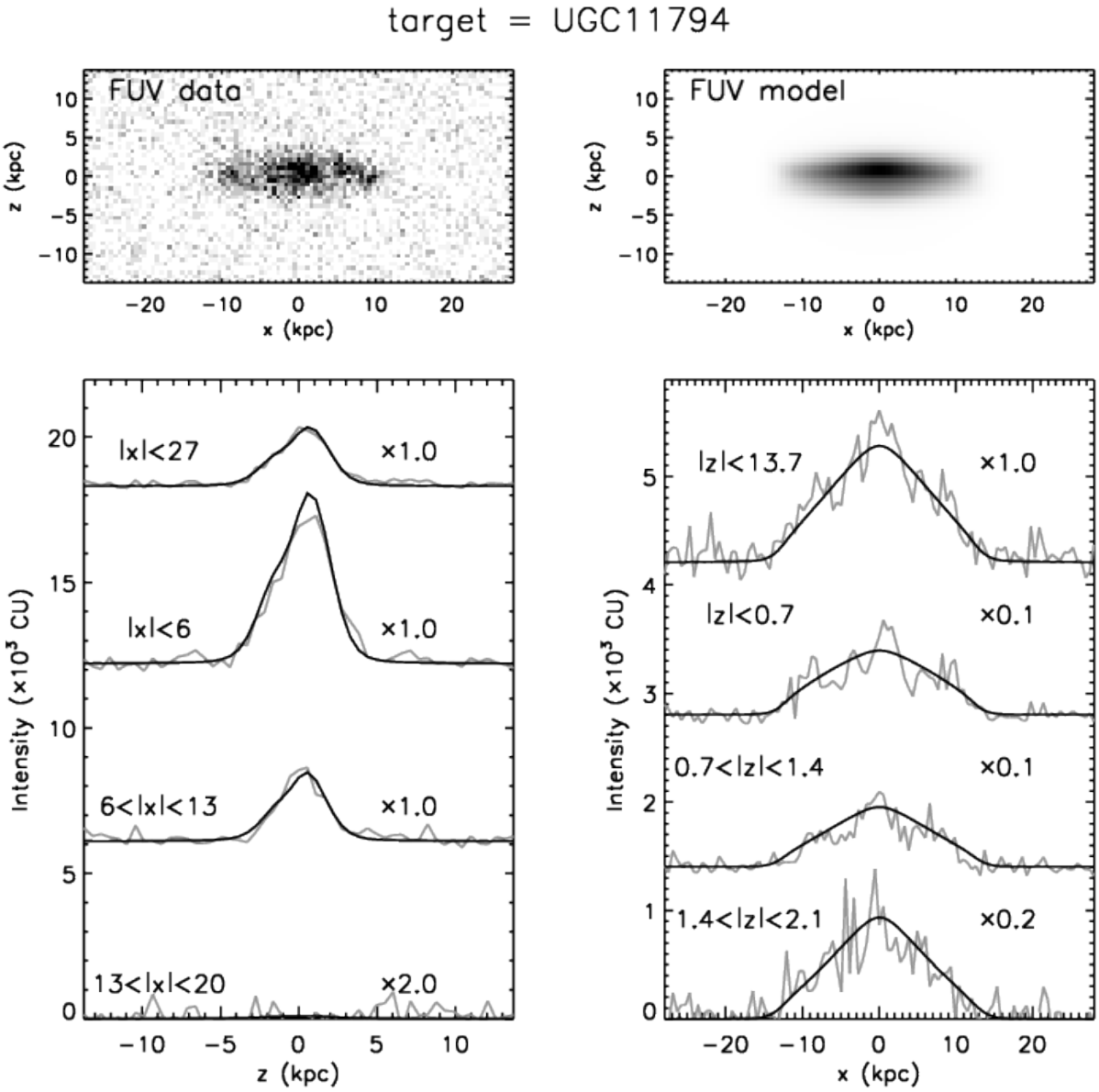

(f)

Fig. 3.— Continued.

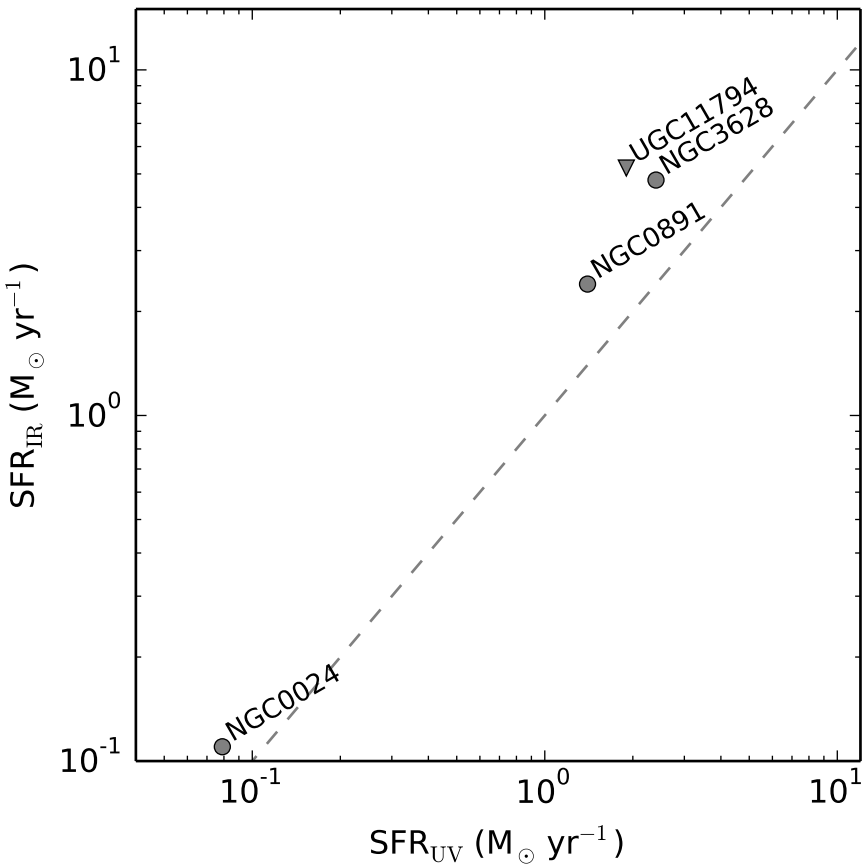

Fig. 4.— Comparison of Star Formation Rate. The SFR_{UV} is from the *GALEX* image fitting (Table 4), while the SFR_{IR} is from the IR luminosity (Table 1). The dashed line indicates the 1-to-1 ratio. This plot shows only the targets that have the SFR_{IR} information (cf. Table 1). The downward triangle indicates the upper limit of SFR_{IR}.

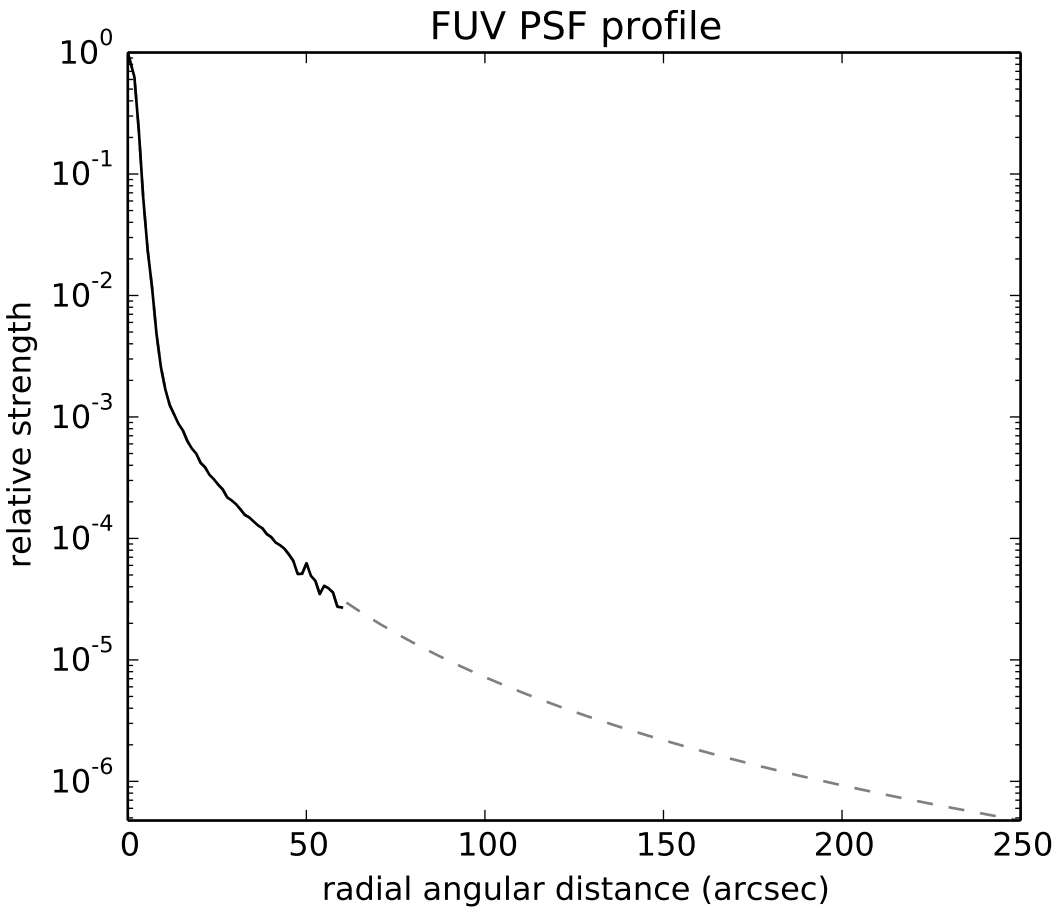

Fig. 5.— The average radial profile of *GALEX* FUV-band PSF (*solid*) and the extrapolated wing part (*dashed*).

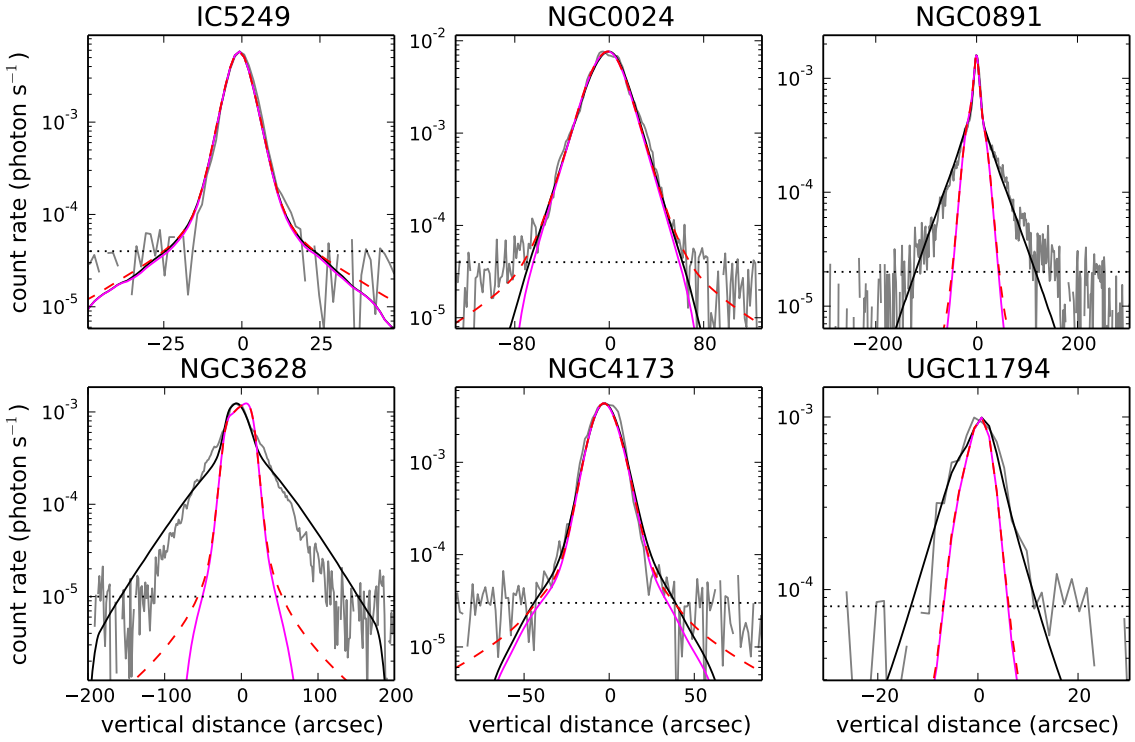

Fig. 6.— The effects of the extended PSF on the model fitting. All lines are the horizontally averaged vertical profiles. The *gray-solid line* is from the *GALEX* FUV data. The *black-solid line* is from the best-fit model convoluted with the *standard* PSF. The *magenta-solid and red-dashed lines* are from the best-fit model convoluted with the *standard* and *extended* PSF, respectively, excluding the thick dust disk component (see eq. (1)). The *dotted line* indicates the upper bound of background noise.

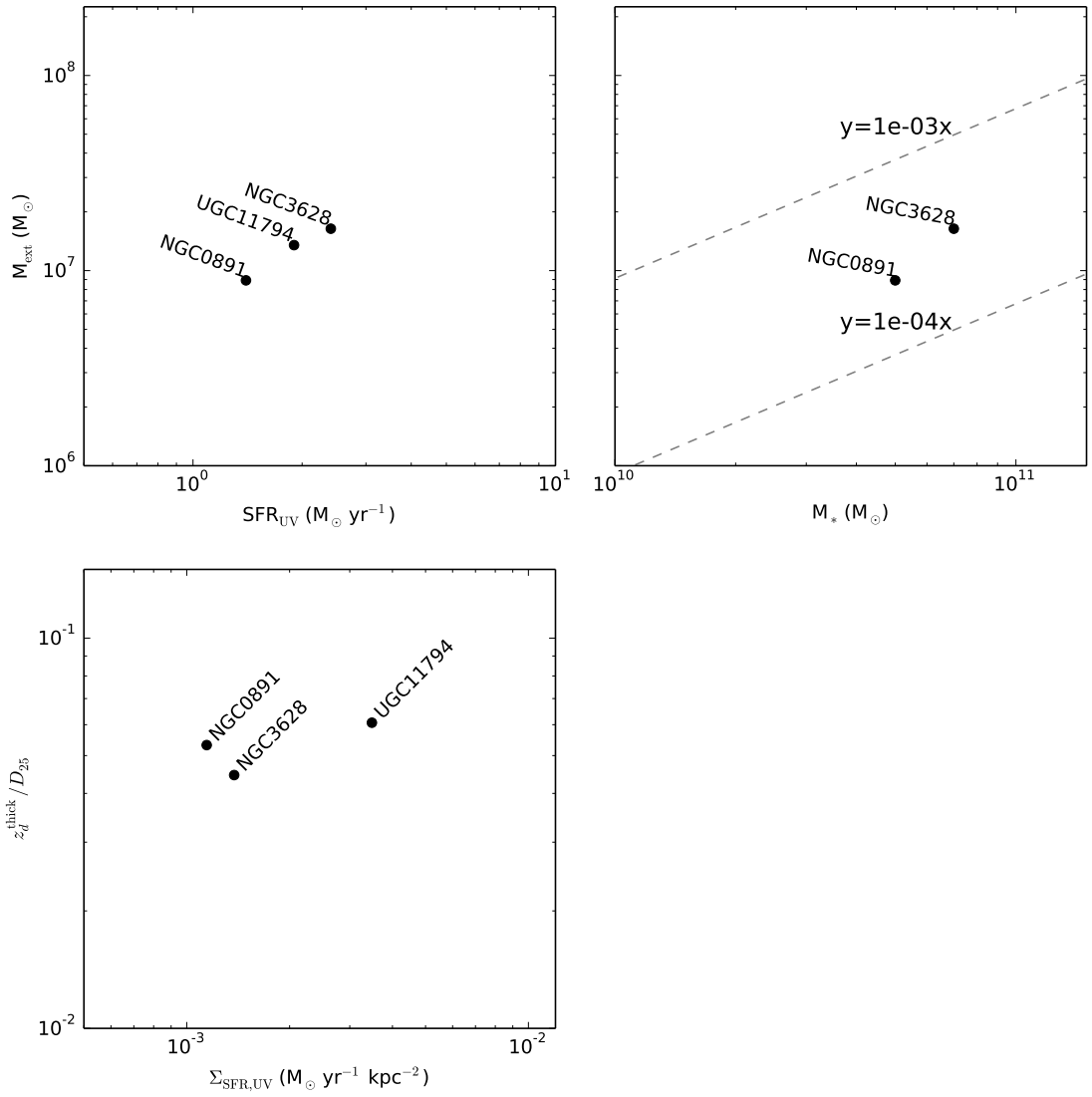

Fig. 7.— Relation between Physical Parameters from the Model Fitting. The scatter plots of the extraplanar dust mass (dust mass of $|z| > 5\% \times D_{25}$) with the star formation rate (*upper-left*) and the stellar mass (*upper-right*). The stellar mass is from Table 1. The guide lines are shown in the *upper-right* panel. (*lower-left*) The scatter plot between the star formation rate surface density and the ratio of the thick dust disk scale-height over the major axis size.

Table 1. Target information

Target	Type	i	d	D_{25}	D_{25}	M_*	$\mathrm{SFR_{IR}}$
		($^\circ$)	(Mpc)	($'$)	(kpc)	($10^{10}\,M_\odot$)	($M_\odot$ yr^{-1})
	(1)	(2)	(3)	(4)	(5)	(6)	(7)
IC 5249	SBcd	90	29.70	3.63	31.36	0.15	···
NGC 0024	Sc	70	7.24	5.75	12.12	0.15	0.11
NGC 0891	Sb	90	10.06	13.49	39.48	5.00	2.4
NGC 3628	Sb	79	10.95	14.79	47.11	7.00	4.8
NGC 4173	SBcd	90	7.83	5.01	11.41	···	···
UGC 11794	Sab	78	75.40	1.20	26.36	···	< 5.2

Note. — Columns: (1) morphological type, (2) disk inclination angle, (3) distance to the target, (4)-(5) major axis size, (6) stellar mass, and (7) the star formation rate estimated from the infrared luminosity. Columns (1)-(2) are taken from the HyperLeda galaxy database, `http://leda.univ-lyon1.fr`. Columns (3)-(4) are taken from the NED database, `http://ned.ipac.caltech.edu/`. Column (5) is calculated with Columns (3) and (4). Columns (6)-(7) are taken from Hodges-Kluck & Bregman (2014). Column (6) is computed from the absolute K-band magnitude of 2MASS catalog (Skrutskie et al. 2006) and the color corrections from Bell & de Jong (2001). Column (7) is estimated from the relation between SFR and IR luminosity (Kennicutt 1998). The IR luminosity is measured using the Rice et al. (1988) relation and the *IRAS* catalog.

Table 2. *GALEX* information

Band	Bandwidth (Å)	Effective wavelength (Å)	Field of view (°)	Image resolution (″)	Image pixel scale (″)
FUV	1344–1786	1538.6	1.27	4.2	1.5
NUV	1771–2831	2315.7	1.25	5.3	1.5

Note. — All the information is from Morrissey et al. (2007).

Table 3. *GALEX* Exposure Time

Target	FUV (s)	NUV (s)
IC 5249	1705	4467
NGC 0024	1577	1577
NGC 0891	6047	6283
NGC 4173	1648	1648
NGC 7090	3007	3088

Table 4. Fitting Parameters of the Best Fit for the *GALEX* FUV Images

Target	[a] $z_d^{\rm thin}$ (kpc) (1)	[a] $z_d^{\rm thick}$ (kpc) (2)	$\tau_B^{\rm thin}$ (3)	$\tau_B^{\rm thick}$ (4)	z_s (kpc) (5)	h_d (kpc) (6)	h_s (kpc) (7)	R_d (kpc) (8)	[b] Z_d (kpc) (9)	R_s (kpc) (10)	i (°) (11)	$\rm SFR_{UV}$ ($M_\odot$ yr^{-1}) (12)
IC5249	0.375	2.600	0.562	0.013	0.208	9.3	122.5	15.7	5.0	15.7	90.2	0.57
			(0.333)	(0.218)	(0.025)	(1.0)	(52.5)	(0.7)		(0.5)	(0.3)	(0.19)
NGC0024	0.175	3.100	0.443	1.002	0.146	0.8	1.3	12.5	5.0	12.5	78.1	0.079
			(0.125)	(0.778)	(0.037)	(0.1)	(0.1)	(2.8)		(4.1)	(0.6)	(0.0036)
NGC0891	0.325	2.100	0.985	0.436	0.102	12.0	5.8	16.9	12.0	15.9	89.5	1.4
			(0.412)	(0.285)	(0.014)	(2.0)	(0.9)	(3.2)		(1.6)	(0.4)	(0.34)
NGC3628	0.225	2.100	1.230	0.640	0.164	16.4	7.8	20.0	10.0	19.5	91.6	2.4
			(1.115)	(0.267)	(0.127)	(22.1)	(13.6)	(6.9)		(1.5)	(2.0)	(1.3)
NGC4173	0.125	0.600	0.371	0.093	0.084	2.8	1.2	19.7	5.0	19.2	85.0	0.082
			(0.365)	(0.469)	(0.373)	(2.9)	(1.9)	(13.1)		(10.8)	(6.6)	(0.020)
UGC11794	0.175	1.600	0.747	0.450	0.201	15.3	4.2	18.3	10.0	13.8	91.1	1.9
			(0.686)	(0.227)	(0.174)	(6.2)	(2.9)	(2.5)		(2.9)	(8.0)	(1.7)

Note. — The numbers surrounded by parenthesis in the table body are the corresponding uncertainties derived from the area half z-step away from the best-fit ($z_d^{\rm thin}$,$z_d^{\rm thick}$). Columns: (1) the scale height of the thin dust disk, (2) the scale height of the thick dust disk, (3) the B-band optical depth along the symmetric axis of the thin dust disk, (4) the B-band optical depth along the symmetric axis of the thick dust disk, (5) the scale height of the stellar disk, (6) the scale length of the thin and thick dust disks, (7) the scale length of the stellar disk, (8) the radial extent of the thin and thick dust disks, (9) the vertical extent of the thin and thick dust disks, (10) the radial extent of the stellar disk, (11) the disk inclination angle measured from the top of the image downward (cf. Figure 2), and (12) the star formation rate estimated from the intrinsic ultraviolet luminosity.

[a]We covered several ($z_d^{\rm thin}$, $z_d^{\rm thick}$) grids. See text for detail.

[b]This parameter is fixed during the fitting.

Table 5. Adopted z_x and Estimated M_{ext}

Target	z_x (kpc)	M_{ext} ($M_\odot$)
NGC0891	1.97	8.91e+06
NGC3628	2.36	1.64e+07
UGC11794	1.32	1.35e+07